Direct visualization of the Jahn–Teller effect coupled to Na ordering in $Na_{5/8}MnO_2$

Xin Li[1], Xiaohua Ma[1], Dong Su[2], Lei Liu[1], Robin Chisnell[3], Shyue Ping Ong[1†], Hailong Chen[1†], Alexandra Toumar[1], Juan-Carlos Idrobo[4], Yuechuan Lei[5], Jianming Bai[5], Feng Wang[6], Jeffrey W. Lynn[7], Young S. Lee[3] and Gerbrand Ceder[1]*

The cooperative Jahn–Teller effect (CJTE) refers to the correlation of distortions arising from individual Jahn–Teller centres in complex compounds[1,2]. The effect usually induces strong coupling between the static or dynamic charge, orbital and magnetic ordering, which has been related to many important phenomena such as colossal magnetoresistance[1,3] and superconductivity[1,4]. Here we report a $Na_{5/8}MnO_2$ superstructure with a pronounced static CJTE that is coupled to an unusual Na vacancy ordering. We visualize this coupled distortion and Na ordering down to the atomic scale. The Mn planes are periodically distorted by a charge modulation on the Mn stripes, which in turn drives an unusually large displacement of some Na ions through long-ranged $Na-O-Mn^{3+}-O-Na$ interactions into a highly distorted octahedral site. At lower temperatures, magnetic order appears, in which Mn atomic stripes with different magnetic couplings are interwoven with each other. Our work demonstrates the strong interaction between alkali ordering, displacement, and electronic and magnetic structure, and underlines the important role that structural details play in determining electronic behaviour.

$NaTMO_2$ (TM = $3d$ transition metal ions) compounds with alternating Na and TM layers have been studied extensively for their potential application in rechargeable batteries[5–7] or as the parent materials of the superconductive cobaltate[5,8–10]. Na can be electrochemically and reversibly removed from these materials creating Na_xTMO_2 ($0 < x < 1$) compounds in a process called deintercalation. Superstructures due to Na-vacancy (V_{Na}) ordering have been observed and identified to be dominated by the electrostatic interactions in Na_xVO_2 (ref. 6) and Na_xCoO_2 (refs 5,8). However, Na_xMnO_2 is expected to be more complicated as it mixes Mn^{3+} ions, which exhibit one of the largest Jahn–Teller distortions in transition metal compounds, and forms antiferromagnetic (AF) Mn^{3+} atomic stripes[11–13], with Mn^{4+} ions, which are not Jahn–Teller active and can form ferromagnetic or AF nearest-neighbour couplings, depending on the competition between different direct and indirect exchange mechanisms[14]. As such, Na_xMnO_2 is well suited to study the interplay between the V_{Na} ordering, CJTE and the magnetic properties.

There have been continuous efforts to directly visualize the CJTE using scanning/transmission electron microscopy[3,15–17] (S/TEM).

Here, electron diffraction, synchrotron X-ray diffraction (XRD), density functional theory (DFT) and aberration-corrected atomic-resolution STEM imaging are used to determine the superstructure of electrochemically formed $Na_{5/8}MnO_2$, and to visualize in sodium intercalation compounds the cooperative distortion of the Mn Jahn–Teller centres and their coupling to Na ordering. Rather than being dominated by electrostatic interactions, we show here direct experimental evidence from STEM imaging that the superstructure in $Na_{5/8}MnO_2$ is mainly controlled by Jahn–Teller distortions which induce specific long-ranged $Na–V_{Na}$ interactions through Mn charge and d-orbital orderings. We use neutron powder diffraction, magnetic susceptibility measurements and DFT computations to demonstrate that a 'magnetic stripe sandwich' structure is formed at low temperatures, which causes a pronounced change of the magnetic properties.

Electrochemical Na removal from $NaMnO_2$ initially is known to occur through a two-phase reaction, forming a new phase Na_xMnO_2 (ref. 18). Figure 1a,b shows the structure of conventional monoclinic $NaMnO_2$, which is used to index the electron diffraction patterns of Na_xMnO_2 shown in Fig. 1c–e. The formation of a superstructure is clear from the (200), (1–22), (12–2) diffraction spots. In the Z-contrast image shown in Fig. 2b, each dot corresponds to either a Na or Mn atomic stripe projected along the [010] or b direction. The periodic intensity modulation of one bright and three dark dots in the Na plane is proportional to the Na concentration in these stripes. The superstructure hkl peaks and STEM Z-contrast information efficiently limit the possible Na orderings in this compound. To determine a unique order, we performed an exhaustive search of the possible superstructures in the supercells up to 32 formula units for several x values in Na_xMnO_2. The only superstructure that matches all of the electron diffractions and STEM images occurs at $x = 5/8$. The synchrotron XRD refinement (Supplementary Fig. 1 and Tables 2 and 3) was performed on this particular superstructure model starting with DFT relaxed ion coordinates and shows a good fit. Furthermore, DFT calculations show that this superstructure has the lowest energy among the 300 different Na arrangements that we calculated for $x = 5/8$, with its energy below the tie line connecting the two lowest energy structures at neighbouring Na compositions, indicating that it is thermodynamically stable (Supplementary Fig. 2). On the basis of

[1]Department of Materials Science and Engineering, Massachusetts Institute of Technology, Cambridge, Massachusetts 02139, USA, [2]Center for Functional Nanomaterials, Brookhaven National Laboratory, Upton, New York 11973, USA, [3]Department of Physics, Massachusetts Institute of Technology, Cambridge, Massachusetts 02139, USA, [4]Center for Nanophase Materials Sciences, Oak Ridge National Laboratory, Oak Ridge, Tennessee 37831, USA, [5]National Synchrotron Light Source, Brookhaven National Laboratory, Upton, New York 11973, USA, [6]Sustainable Energy Technologies Department, Brookhaven National Laboratory, Upton, New York 11973, USA, [7]NIST Center for Neutron Research, National Institute of Standards and Technology, Gaithersburg, Maryland 20899, USA. †Present addresses: Department of NanoEngineering, University of California, San Diego, La Jolla, California, USA (S.P.O.); School of Mechanical Engineering, Georgia Institute of Technology, Atlanta, Georgia, USA (H.C.). *e-mail: gceder@mit.edu
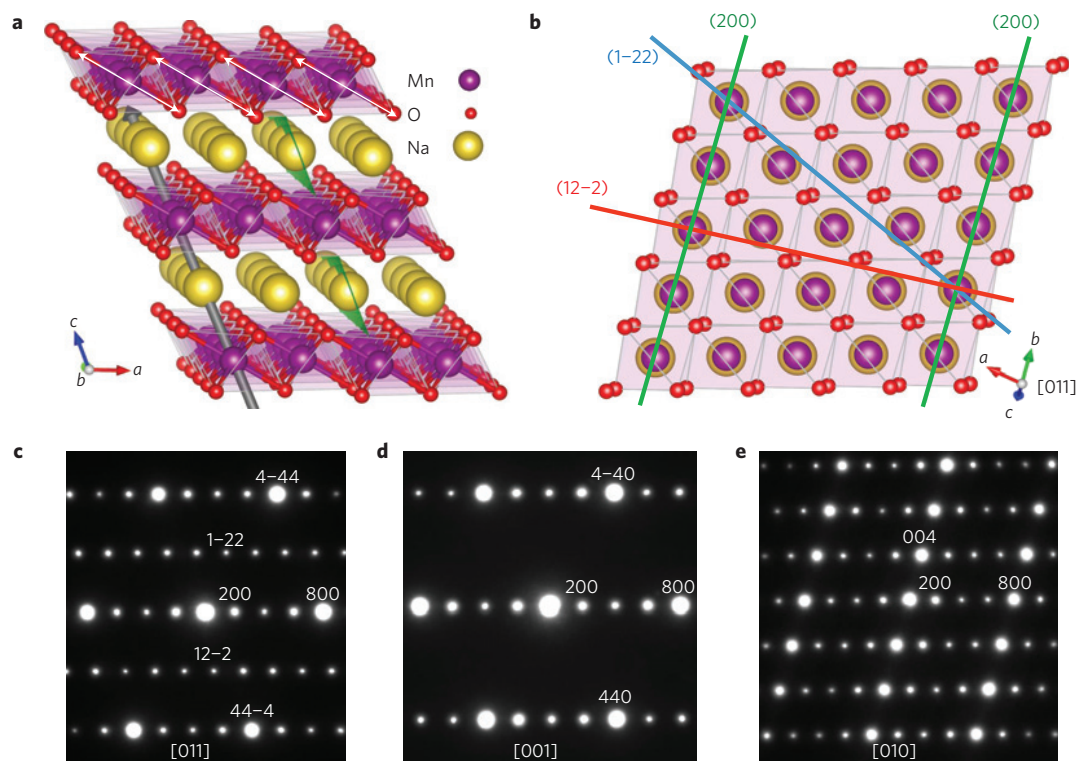
Figure 1 | Superstructure *hkl* spots in electron diffraction patterns show the ordering of Na⁺ in Na$_x$MnO$_2$. a, The monoclinic structure (C2/m) of pristine NaMnO$_2$ with the conventional definition of the lattice parameters. The direction of the Jahn–Teller distortion is marked by the white arrows. The grey arrow shows the [011] direction, and the (200) plane is in green. **b**, Structure looking along [011]. The green, blue and red lines are the [011] projections of (200), (1–22) and (12–2) planes, respectively. **c**–**e**, The experimental electron diffraction patterns along [011], [001] and [010] show consistently the 4-period superstructure diffraction spots corresponding to the (200) planes. The [011] diffraction pattern in **c** shows additional 2-period (1–22) and (12–2) superstructure diffraction spots.

the experimental and computational data, we conclude that this Na$_{5/8}$MnO$_2$ superstructure is the new phase formed in the first voltage plateau when Na is de-intercalated from NaMnO$_2$ (ref. 18). It is worth noting that the Na-vacancy arrangement with the lowest electrostatic energy (labelled as Ewald_0 in Supplementary Fig. 2) at $x = 5/8$ is significantly higher in energy, indicating that the electrostatic interactions do not dominate in this structure.

We now describe the structure and its magnetic ordering in more detail. The Na layer of Na$_{5/8}$MnO$_2$ is formed by one full Na atomic stripe parallel to three half-full Na stripes in which Na and V$_{Na}$ alternate, as shown in Figs 2b, 3a and 4a,b from three different zone axes, respectively. We observe Mn charge ordering in both the STEM-EELS (electron energy loss spectroscopy) measurement in Fig. 2, where the L$_3$/L$_2$ peak ratio is inversely proportional to the Mn charge state, and the DFT calculations in Fig. 3. There are three types of Mn atomic stripe: a pure Mn^{3+} stripe, a pure Mn^{4+} stripe and a stripe of alternating Mn^{3+} and Mn^{4+} ions. As the Mn^{3+}O$_6$ octahedron is Jahn–Teller distorted and the Mn^{4+}O$_6$ is not, the periodic arrangement of these different stripes gives a CJTE, which can be directly visualized by the rippling of the Mn layers in Fig. 2b. It is worth noting that in the DFT-calculated structure Na ions in one of the three half-full Na stripes are displaced along the stripe direction [010] by about 1.4 Å from their normal octahedral site into a new site, consistent with our synchrotron XRD refinement. This stripe is labelled as Na$_{Disp}$ in Figs 2 and 3 and as stripe 'e' in Fig. 4. The local environment of the displaced Na ions (Na$_{Disp}$), shown in Fig. 3b, is a highly distorted octahedral site face-sharing with both Mn^{4+}O$_6$ octahedra. Although such face-sharing sites occur in the O1 structure of CoO$_2$ or NiO$_2$ when they are fully delithiated[19], it is unusual to see such a site occupied by an alkali ion, as we find in Na$_{5/8}$MnO$_2$. The other two types of Na site in Na$_{5/8}$MnO$_2$, Na$_2$ and

Na$_3$, are normal slightly distorted octahedral sites, which edge-share with both TM layers. Figure 3c clearly shows that notwithstanding the unusual site occupation for Na$_{Disp}$ the stacking is still O3 type[20].

The Na$_{Disp}$ is directly observed in the STEM measurement in Fig. 4. The annular bright field (ABF) image is sensitive to light elements such as Na, and can visualize the Na$_{Disp}$ ions between the neighbouring Mn columns, as shown along the stripe labelled 'e' in Fig. 4a, as well as in its line scan in Fig. 4e. The Na intensity modulations along the other stripes labelled as 'c,d' in the ABF image and their corresponding line scans in Fig. 4c,d, respectively, are also consistent with the $x = 5/8$ superstructure model. The type of each atomic column in the ABF image was identified by direct comparison with the annular dark field (ADF) image taken simultaneously (Fig. 4b) with consistent contrast information.

To investigate the role of the Jahn–Teller distortion on the displacement of the Na$_{Disp}$ ions, we replaced all of the Mn ions by non-Jahn–Teller-active Cr ions in the DFT calculation, which reduced the Na displacement to less than 0.5 Å, indicating that the Na shift is largely driven by the Jahn–Teller distortion. The Na and V$_{Na}$ ordering is in fact connected by the cooperative Jahn–Teller effect to the Mn^{3+} and Mn^{4+} in a remarkable way. At the extension of all 180° –O–Mn–O– triplets are Na sites in Na$_{5/8}$MnO$_2$. It has previously been argued in the Li$_x$NiO$_2$ system that the Jahn–Teller activity of the transition metal creates attractive interactions between the alkali ions sitting at the extensions of these 180° oxygen–metal–oxygen bonds due to the *spd* hybridization of the alkali-*s*, O-*p* and metal-d_{z^2} orbitals[21]. The inset of Fig. 2b (enlarged in Supplementary Fig. 3a) shows that in Na$_{5/8}$MnO$_2$ all of the non-displaced Na ions are in this configuration. In the (202) planes, these 180° Na–O–Mn^{3+}–O–Na fragments alternate with non-Jahn–Teller-distorted V$_{Na}$–O–Mn^{4+}–O–V$_{Na}$ configurations, as
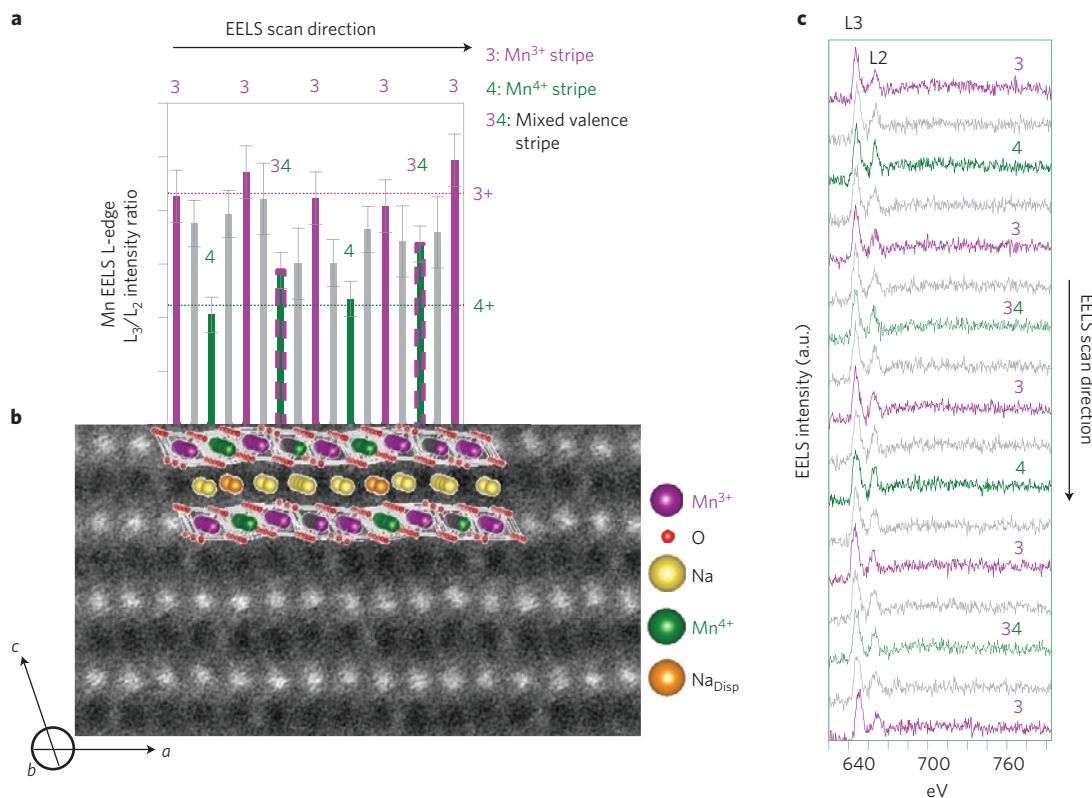
Figure 2 | Atomic-resolution STEM image visualizes CJTE and STEM-EELS shows Mn charge ordering. a, The Mn EELS L_3/L_2 peak ratio at each Mn [010] atomic column site along the STEM-EELS scanning direction of [100]. The dashed lines show the ratios corresponding to the standard samples of Mn_2O_3 and MnO_2. The error bars are determined from the errors introduced in background subtraction and data fluctuation among spectra. **b**, STEM image along [010] shows the periodic distortion of the Mn ab plane and the intensity modulation of the Na plane that agrees quantitatively with the superstructure model. **c**, The 17 Mn L_{23}-edge EEL spectra after background subtraction that give the L3/L2 ratios shown in **b**.

shown in Supplementary Fig. 3b. The origin of the displacement of the Na_{Disp} ions in the remaining half-full stripe is now clear (see Fig. 3d and Supplementary Fig. 3c): there are not enough Na ions in this stripe to create only 180° $Na–O–Mn^{3+}–O–Na$ configurations. Hence, rather than create $V_{Na}–O–Mn^{3+}–O–Na$ configurations, the Na ions relax to the highly distorted octahedral site where they share the symmetric attraction of the two neighbouring Jahn–Teller-distorted $–O–Mn^{3+}–O–Na$ configurations. In other words, the Jahn–Teller-distorted 180° configuration of $V_{Na}–O–Mn^{3+}–O–Na$ is unstable, producing a long-ranged $V_{Na}–Na$ repulsion through the Jahn–Teller centre. We have also re-examined the previously predicted superstructures in Li_xNiO_2 (refs 21,22), and found no 180° $V_{Li}–O–Ni^{3+}–O–Li$ configurations. As many new battery compounds are based on the Mn^{4+}/Mn^{3+} redox couple, the argument of Jahn–Teller-mediated orbital interactions has general implications for both Na and Li batteries[23,24].

One of the interesting consequences of the electronic and alkali ordering in $Na_{5/8}MnO_2$ is that it leads to a new magnetic ordering. On the basis of neutron powder diffraction, magnetic susceptibility measurements and DFT generalized gradient approximation $(GGA) + U$ calculations, we propose the magnetic-stripe-sandwich structure at low temperature in Fig. 3a. The DFT total energies for different collinear magnetic spin orderings in $Na_{5/8}MnO_2$ in a supercell containing up to 80 formula units were calculated, and mapped onto a spin Hamiltonian, $- \sum_{i<j} J_{ij} S_i \cdot S_j$, to extract the nearest-neighbour and next-nearest-neighbour spin exchange parameters J_{ij} between site i and j, as defined in Fig. 3a. S_i and S_j are the spin angular momentum operators; details of this method can be found in the literature[12]. The resulting exchange parameters and ground-state magnetic structures in Supplementary Table 1 predict the Mn^{3+} stripes to be AF, Mn^{4+} stripes to be ferrimagnetic,

and mixed valence Mn^{3+}/Mn^{4+} stripes to be ferrimagnetic with AF nearest-neighbour coupling, at $U = 2.47$ eV, a U value close to the previously determined one by comparison of the GGA + U DFT simulation of the pristine $NaMnO_2$ (ref. 12) with neutron powder diffraction[11,13].

The neutron powder diffraction data of $Na_{5/8}MnO_2$ shown in Fig. 5 confirm the presence of long-range magnetic order at low temperatures. The diffraction pattern taken at $T = 2.5$ K reveals additional magnetic Bragg peaks compared with the diffraction pattern at $T = 100$ K (consisting of nuclear Bragg peaks from the crystal structure). The inset in Fig. 5 shows the temperature dependence of the integrated intensity of the lowest angle magnetic Bragg peak, indicating an ordering temperature of around $T \sim 60$ K that is consistent with the temperature of the upturn in the magnetic susceptibility. The DFT-calculated coupling constant of -61.5 K (negative value corresponds to AF interaction) for the Mn^{3+} AF stripe at $U = 2.47$ eV (Supplementary Table 1) is in reasonable agreement with the temperature scale of the observed ordering.

The intensities of the magnetic Bragg peaks can be described by a pattern of magnetic stripes of ordered moments on the Mn sites. The simplest model of ordered moments consistent with the data consists of AF stripes of Mn^{3+} with an AF coupling between stripes, as indicated by the blue arrows in Fig. 3a. When only these moments are taken into account, the fits yield an ordered moment of 3.2(4) μ_B per Mn^{3+}. Other magnetic ordering patterns that have the same periodicity as these AF Mn^{3+} stripes would also be consistent with the data. For example, AF stripes of Mn^{4+} and mixed Mn^{3+}/Mn^{4+} coexisting with the AF stripes of Mn^{3+} would yield a similar magnetic diffraction pattern, but the average moment would have a smaller value of 2.2(3) μ_B per Mn. Further details of the magnetic structure will probably require measurements on
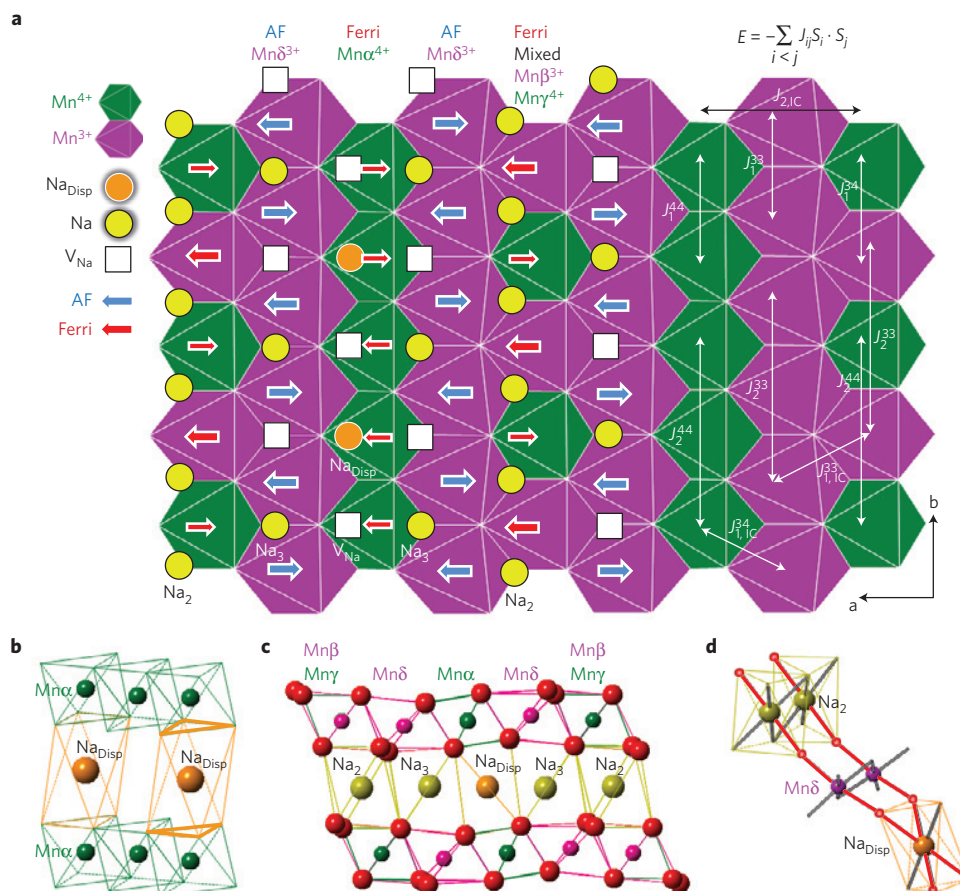
Figure 3 | Na$_{5/8}$MnO$_2$ superstructure shows V$_{Na}$ ordering, Mn charge and magnetic stripe orderings. a, The Na ordering in the ab layer includes Na ions (yellow circles), displaced Na ions (orange circles labelled with Na$_{Disp}$) and Na vacancies (open squares). The TM layer charge ordering includes pure Mn^{3+}O$_6$ (purple hexagon) stripes, pure Mn^{4+}O$_6$ (green hexagon) stripes and the mixed-valence Mn stripes. The magnetic spin stripe ordering includes ferrimagnetic stripes (red arrows) and AF stripes (blue arrows). The exchange parameters J_{ij} between different Mn sites provided in Supplementary Table 1 are defined. The different sites labelled by Mn(α–δ), Na(Disp, 2, 3) and O(1–6) correspond to Supplementary Tables 2 and 3. **b**, The local environment of two displaced Na ion face-sharing with the Mn^{4+}O$_6$ octahedra. The two triangles that share faces with one Na site are labelled with thick lines. **c**, The structure viewed from the b direction shows oxygen O3 stacking. **d**, The basic unit of the spd hybridization interaction that drives the Na displacement to the distorted octahedral site. The spd hybridized bonds are in red connecting Na, O and Mn^{3+} ions.

single crystals. Interestingly, the divergence of the field-cooled and zero-field-cooled susceptibility curves around $T = 12$ K in Supplementary Fig. 4 may indicate the presence of weakly coupled ferrimagnetic components and agrees quantitatively with the calculated nearest-neighbour coupling constant of 11.9 K for the Mn^{4+} ferrimagnetic stripes at $U = 2.47$ eV (Supplementary Table 1). Overall, the general pattern predicted by DFT of AF Mn^{3+} stripes interwoven with the Mn^{4+} and Mn^{4+}/Mn^{3+} stripes is fully supported by the experiments.

This new magnetic-stripe-sandwich structure may have potential application in magnetic storage or spin electronics[25] as the one-dimensional analogy to the sandwich structure of two-dimensional magnetic thin films, from which abundant magnetic phenomena have been engineered[25]. It is also worth noting that the dynamic version of the hole-segregated magnetic stripes has been proposed to be important for high-temperature cuprate superconductors[26].

We have found Na$_{5/8}$MnO$_2$ to be a model system for visualizing the complex interactions between Na ion ordering, charge ordering, magnetic ordering and cooperative Jahn–Teller distortions. We find that in contrast to other alkali-vacancy systems the Na ordering in Na$_x$MnO$_2$ is controlled by the underlying combination of electrostatic and electronic structure interactions through the Jahn–Teller effect, which enables some Na to occupy the highly distorted octahedral site. This leads to Na and Mn charge-ordered

stripes, which in turn yields a fascinating low-temperature magnetic ordering to develop. DFT and experimental observations are in excellent agreement, providing confidence in the proposed ground state and in the explanation for the physical origin of its stability. The understanding of the CJTE here may have general implications for understanding complex compounds where the Jahn–Teller effect is prominent, including intercalation energy storage materials and high-temperature superconductors, and illustrates the fascinating physics of mixed Mn valence systems.

Methods

Synthesis. The pristine NaMnO$_2$ powder was synthesized by the solid-state reaction, and the electrochemical cells were configured on the basis of our previous publication[18]. The Na$_{5/8}$MnO$_2$ cathode films were obtained by charging to the end of the first electrochemical plateau either by the C/200 galvanostatic charge in a home-made *in situ* XRD cell to monitor the depletion of the pristine phase or by the potentiostatic intermittent titration technique charge with 10 meV step up to 2.685 V in a Swagelok cell. The charged batteries were disassembled in a glove box with the cathode films dried for further characterizations. The Na$_{5/8}$MnO$_2$ powder for the neutron diffraction was obtained by chemical de-intercalation of pristine NaMnO$_2$ powder in an iodine acetonitrile solution.

TEM. TEM samples were made by sonication of the charged cathode films in anhydrous dimethyl carbonate inside a glove box, and sealed in airtight bottles before immediate transfer into the TEM column. The electron diffractions were
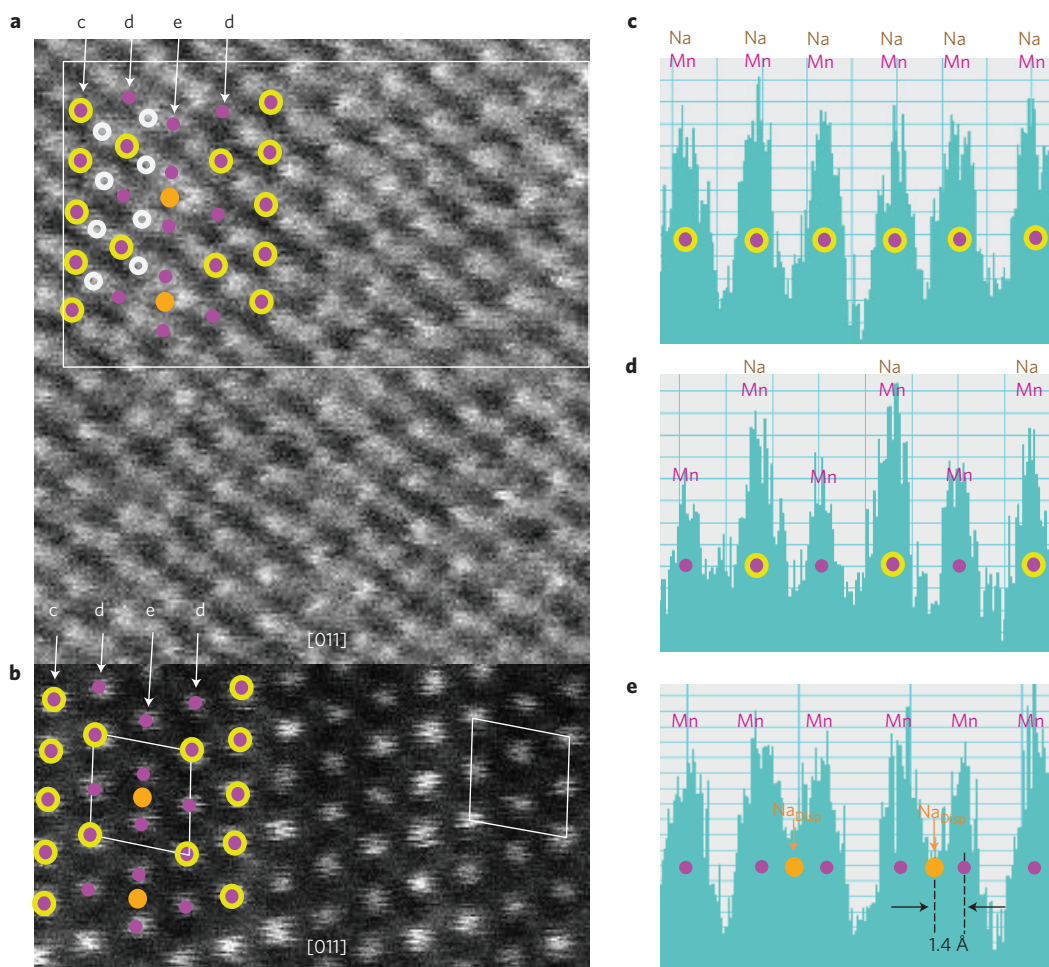
Figure 4 | The Na ordering in Na$_{5/8}$MnO$_2$ is visualized by STEM ABF and ADF images. a,b, Simultaneously taken STEM-ABF (**a**) and ADF (**b**) images along the [011] zone axis. The corresponding region to the ADF image is marked by the white rectangle in the ABF image. The ADF image is taken at the optimum defocus condition, which is a defocus value for the ABF image with inversed contrast to the optimum focus condition (details in Methods). **c–e,** STEM-ABF line scans along the directions marked by the white arrows in **a**. The label and model of Mn and/or Na show the projected atomic columns at each intensity peak position, corresponding to the superposed model in **a**, where the white circles are for the oxygen columns.

taken on the JEOL 2010F at MIT. The STEM-ABF/ADF and EELS line scan were taken on the Cs-corrected cold field-emission Hitachi HD 2700C at 200 kV at Brookhaven National Laboratory (BNL). The STEM images were obtained by using 1 Å scanning probe of 28 mrad semi-convergence angle, with the semi-collection angles of 10–22 mrad and 53–280 mrad for the ABF and ADF detectors, respectively. The STEM ABF and ADF images were taken simultaneously at the optimal defocus value of the ADF imaging condition, which was more defocused than the optimal ABF imaging condition on this instrument. Thus, the contrast in the ABF image is reversed with the bright area corresponding to the atomic positions[27]. The line-scanned EELS were collected by a 1.4 Å probe of 60 pA probe current and taken by the Gatan Enfina ER spectrometer with the semi-collection angle of 20 mrad at 0.3 eV per channel, 1.4 Å scanning interval and 1.2 s collection time per spectrum. The Mn L$_{2,3}$ edges were fitted by the Gaussian model after a background subtraction of power law.

XRD. The charged cathode film was sealed with silicone tape for the collection of the synchrotron XRD pattern on beam line X14A at NSLS at BNL with a wavelength of 0.7788 Å. The XRD refinement was done by GSAS software with the background estimated by a shifted Chebyschev function and the peak profile described by the Finger, Cox and Jephcoat function. The preferential orientation was set for the first (004) peak. The Na$_{5/8}$MnO$_2$ powder was sealed in the capillary for the synchrotron XRD measurement on X14A at NSLS, which confirmed the same superstructure phase as the electrochemically de-intercalated cathode film.

Neutron diffraction and magnetic susceptibility. Neutron diffraction measurements were performed on 5 g of chemically de-intercalated Na$_{5/8}$MnO$_2$ powder using the triple-axis spectrometer BT-7 at the NIST Center for Neutron

Research[28]. Measurements were taken in two-axis mode with a fixed initial neutron energy of 14.7 meV (wavelength 2.359 Å), collimator configuration open-80'-sample-80' and a radial-position sensitive detector. Magnetic Bragg peaks are observed when the sample was cooled below $T \sim 60$ K. The intensities of the observed magnetic peaks are consistent with a pattern of AF stripes, as discussed in the text. The magnetic structure factors were calculated assuming the spins were collinear and pointing in the direction of the Jahn–Teller-distorted axis of the oxygen octahedra. The form factor was assumed to be that of the free Mn^{3+} ion[29]. The size of the ordered moment can be obtained by comparing the structure factors for the four intense structural peaks in the range $48° < 2\Theta < 63°$ to the integrated intensities of the measured peaks. The structure factor for the structural peaks was calculated assuming the structure obtained from the XRD refinement. The magnetic susceptibility measurements were obtained using a Quantum Design MPMS-XL SQUID.

DFT. All DFT calculations in this work were performed using the Vienna *Ab initio* Simulation Package within the projector augmented-wave approach using the Perdew–Burke–Ernzerhof GGA functional and the GGA+U extension to it. A plane-wave energy cutoff of 520 eV and a k-point density of at least 1,000 per number of atoms in a unit cell were used to ensure that all calculations were converged to within 1 meV atom^{-1}. All calculations were spin-polarized and started from a high-spin configuration. A U value of 3.9 eV was used for Mn for the structure relaxation, in line with previous literature[30]. The phase diagram construction and analysis in Supplementary Fig. 2 was performed using the Python Materials Genomics (pymatgen) library[30]. For the extraction of spin exchange parameters, the magnetic structures were calculated in the supercells with up to 80 formula units, with different U values ranging from 0 eV to 3.9 eV and were converged to 0.01 meV per supercell.
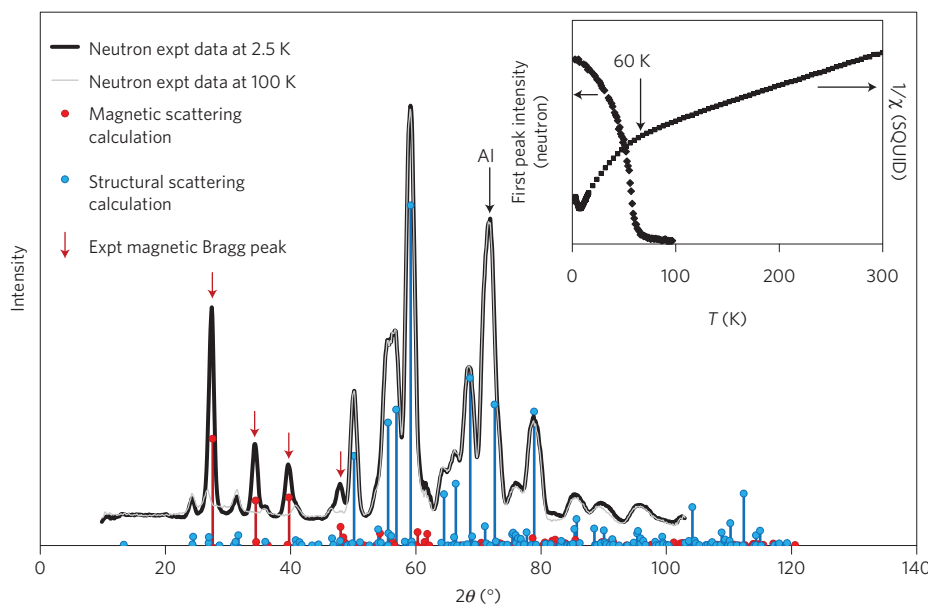
Figure 5 | Neutron diffraction and magnetic susceptibility measurement indicates magnetic stripe ordering. Magnetic Bragg peaks labelled by red arrows are seen in the 2.5 K spectrum compared with the 100 K spectrum. The inset shows the integrated intensity of the strongest magnetic peak in the neutron spectrum (left scale) and also the inverse magnetic susceptibility (right scale) versus temperature. The intensity of the neutron scattering calculation scales with $|F(hkl)|^2/\sin(\theta)/\sin(2\theta)$, where F is the structure factor and 2θ is the scattering angle.

References

1. Bersuker, B. I. *The Jahn–Teller Effect* 1–616 (Cambridge Univ. Press, 2006).
2. Goodenough, J. Jahn–Teller phenomena in solids. *Annu. Rev. Mater. Sci.* **28,** 1–27 (1998).
3. Raveau, B., Hervieu, M., Maignan, A. & Martin, C. The route to CMR manganites: what about charge ordering and phase separation? *J. Mater. Chem.* **11,** 29–36 (2001).
4. Han, J. E., Gunnarsson, O. & Crespi, V. H. Strong superconductivity with local Jahn–Teller phonons in C60 solids. *Phys. Rev. Lett.* **90,** 167006 (2003).
5. Berthelot, R., Carlier, D. & Delmas, C. Electrochemical investigation of the P2–Na$_x$CoO$_2$ phase diagram. *Nature Mater.* **10,** 74–80 (2011).
6. Guignard, M. *et al.* P2-Na$_x$VO$_2$ system as electrodes for batteries and electron-correlated materials. *Nature Mater.* **12,** 74–80 (2013).
7. Yabuuchi, N. *et al.* P2-type Na$_x$[Fe$_{1/2}$Mn$_{1/2}$]O$_2$ made from earth-abundant elements for rechargeable Na batteries. *Nature Mater.* **11,** 512–517 (2012).
8. Roger, M. *et al.* Patterning of sodium ions and the control of electrons in sodium cobaltate. *Nature* **445,** 631–634 (2007).
9. Zandbergen, H. W., Foo, M., Xu, Q., Kumar, V. & Cava, R. J. Sodium ion ordering in Na$_x$CoO$_2$: Electron diffraction study. *Phys. Rev. B* **70,** 024101 (2004).
10. Huang, F-T. *et al.* Scanning transmission electron microscopy using selective high-order Laue zones: Three-dimensional atomic ordering in sodium cobaltate. *Phys. Rev. Lett.* **105,** 125502 (2010).
11. Stock, C. *et al.* One-dimensional magnetic fluctuations in the spin-2 triangular lattice α-NaMnO$_2$. *Phys. Rev. Lett.* **103,** 077202 (2009).
12. Wu, F., Yu, G., Xu, D. & Kan, E. First-principles investigations on the magnetic structure of α-NaMnO$_2$. *J. Phys. Condens. Matter* **24,** 456002 (2012).
13. Giot, M. *et al.* Magnetoelastic coupling and symmetry breaking in the frustrated antiferromagnet α-NaMnO$_2$. *Phys. Rev. Lett.* **99,** 247211 (2007).
14. Masquelier, C. *et al.* Chemical and magnetic characterization of spinel materials in the LiMn$_2$O$_4$–Li$_2$ Mn$_4$O$_9$–Li$_4$Mn$_5$O$_{12}$ system. *J. Solid State Chem.* **123,** 255–266 (1996).
15. Borisevich, A. Y. *et al.* Suppression of octahedral tilts and associated changes in electronic properties at epitaxial oxide heterostructure interfaces. *Phys. Rev. Lett.* **105,** 087204 (2010).
16. Jia, C. L. *et al.* Oxygen octahedron reconstruction in the SrTiO$_3$/LaAlO$_3$ heterointerfaces investigated using aberration-corrected ultrahigh-resolution transmission electron microscopy. *Phys. Rev. B* **79,** 081405(R) (2009).
17. Barrier, N., Lebedev, O. I., Seikh, M. M., Porcher, F. & Raveau, B. Impact of Mn^{3+} upon structure and magnetism of the perovskite derivative Pb$_{2-x}$Ba$_x$FeMnO$_5$ ($x\sim0.7$). *Inorg. Chem.* **52,** 6073–6082 (2013).
18. Ma, X., Chen, H. & Ceder, G. Electrochemical properties of monoclinic NaMnO$_2$. *J. Electrochem. Soc.* **158,** A1307 (2011).
19. Tarascon, J. M. *et al. In situ* structural and electrochemical study of Ni$_{1-x}$Co$_x$O2 metastable oxides prepared by soft chemistry. *J. Solid State Chem.* **147,** 410–420 (1999).
20. Delmas, C., Fouassier, C. & Hagenmuller, P. Structural classification and properties of the layered oxides. *Phys. B+C* **99,** 81–85 (1980).
21. Arroyo y de Dompablo, M. E., Van der Ven, A. & Ceder, G. First-principles calculations of lithium ordering and phase stability on Li$_x$NiO$_2$. *Phys. Rev. B* **66,** 064112 (2002).
22. Peres, J., Weill, F. & Delmas, C. Lithium vacancy ordering in the monoclinic Li$_x$NiO$_2$ ($0.50<x<0.75$) solid solution. *Solid State Ion.* **116,** 19–27 (1999).
23. Kubota, K., Kaneko, T., Yabuuchi, N., Hara, R. & Komaba, S. Electrode performance of lithium containing layered sodium iron manganese oxides for rechargeable Na-ion batteries. 224th ECS Meeting. Sodium-ion Batteries—Cathodes 1 (2013).
24. Lu, Z., MacNeil, D. D. & Dahn, J. R. Layered cathode materials Li[Ni$_x$Li$_{1/3-2x/3}$Mn$_{2/3-x/3}$]O$_2$ for lithium-ion batteries. *Electrochem. Solid-State Lett.* **4,** A191–A194 (2001).
25. Chappert, C., Fert, A. & Van Dau, F. N. The emergence of spin electronics in data storage. *Nature Mater.* **6,** 813–823 (2007).
26. Vojta, M. Lattice symmetry breaking in cuprate superconductors: stripes, nematics, and superconductivity. *Adv. Phys.* **58,** 699–820 (2009).
27. Lee, S., Oshima, Y., Hosono, E., Zhou, H. & Takayanagi, K. Reversible contrast in focus series of annular bright field images of a crystalline LiMn$_2$O$_4$ nanowire. *Ultramicroscopy* **125,** 43–48 (2013).
28. Lynn, J. W. *et al.* Double-focusing thermal triple-axis spectrometer at the NCNR. *J. Res. NIST* **117,** 61–79 (2012).
29. Shirane, G., Shapiro, S. M. & Tranquada, J. M. *Neutron Scattering with a Triple-Axis Spectrometer: Basic Techniques* (Cambridge Univ. Press, 2002).
30. Ong, S. P. *et al.* Python Materials Genomics (pymatgen): A robust, open-source python library for materials analysis. *Comput. Mater. Sci.* **68,** 314–319 (2013).

Author contributions

G.C. planned the study and supervised all aspects of the research. X.L. and G.C. wrote the manuscript. X.L. performed the electron diffraction measurement and DFT calculation, and solved the Na vacancy superstructure. X.L. calculated the spin exchange parameters by DFT and predicted the magnetic structure. X.M. and Y.L. synthesized the pristine compound. X.M. and X.L. obtained the superstructure phase by electrochemistry. X.L. and D.S. performed the STEM measurement and analysed together with J.C.I. the STEM results. L.L. and X.L. synthesized the superstructure phase by chemical de-intercalation.

J.W.L. took the magnetic neutron diffraction data and order parameter, and R.C. and Y.S.L. solved the magnetic structure. X.L. took the magnetic susceptibility data. S.P.O. and A.T. calculated the phase diagram by DFT. J.B. and F.W. took the synchrotron XRD data. H.C., J.B. and X.L. performed the synchrotron XRD refinement. All authors discussed the results and commented on the manuscript.

Additional information

Supplementary information is available in the online version of the paper. Reprints and permissions information is available online at www.nature.com/reprints. Correspondence and requests for materials should be addressed to G.C.

Competing financial interests

The authors declare no competing financial interests.